PHYSICAL REVIEW B **109**, 195408 (2024)

Quarter-quantized thermal Hall effect with parity anomaly

Yu-Hao Wan[1] and Qing-Feng Sun[1,2,*]

[1]*International Center for Quantum Materials and School of Physics, Peking University, Beijing 100871, China*
[2]*Hefei National Laboratory, Hefei 230088, China*

(Received 23 January 2024; accepted 16 April 2024; published 2 May 2024)

We show that in the proximity of s-wave superconductors, the magnetic topological surface states can transform into the Majorana surface state, featuring a single gapless Majorana cone with a parity anomaly when the superconducting pairing gap matches the surface magnetization gap. The emergence of an $N = 1/2$ Majorana chiral edge current is observed at the boundaries between the gap region and the gapless region. Additionally, in systems with a single gapless Majorana cone, a quarter-quantized thermal Hall conductance appears under the dephasing. By mapping the system to a conductor-network model, we identify the appearance of $1/4$ chiral heat channels as the cause of the quarter-quantized Hall thermal conductance. We observe the stability of this quarter-quantized thermal conductance under temperature variations, serving as a distinctive feature indicating the presence of a single gapless Majorana cone in the system. Our models can be experimentally realized using magnetic topological insulators or iron-based superconductors.

DOI: 10.1103/PhysRevB.109.195408

I. INTRODUCTION

Finding a single gapless Dirac cone of fermions has been a persistent problem in condensed matter physics [1–3]. Massless Dirac fermions possess parity symmetry, and the coupling with gauge fields introduces an infinitesimally small mass term to break parity symmetry through a regularization process, which results in the emergence of a Chern-Simons theory, known as the parity anomaly [4–6]. In recent years, various systems with a single gapless Dirac cone have been proposed to investigate the parity anomaly [7–17]—for example, the Haldane model achieving a single massless Dirac fermion by finely tuning the band gap of one valley to close in a honeycomb lattice, while keeping another valley open [18]. Another remarkable approach involves semimagnetic topological insulators. In this system, a gapped Dirac cone emerges on one surface due to the breaking of the local time reversal symmetry, while the Dirac cone on the opposite surface remains gapless [16]. In systems with a single gapless Dirac cone, the parity anomaly leads to a half-integer quantized Hall conductance, as predicted by the anomaly-induced Chern-Simons theory [6,18–20]. Recently, experimental observations have confirmed the existence of half-integer Hall conductance in semimagnetic topological insulators [21]. To describe systems where both massive and massless Dirac fermions coexist, a concept known as the "parity anomaly semimetal" has been proposed [22]. However, all previous models have been based on electronic systems, and the exploration of how to realize the parity anomaly in Majorana systems has yet to be investigated.

The Majorana fermion can be interpreted as the splitting of a complex fermionic field of an electron into real and imaginary parts [23]; thus the massless Majorana fermion also satisfies the Dirac equation. While Majorana systems cannot couple with electromagnetic gauge fields, they can couple with gravity fields [24]. When a massless Majorana fermion couples with a gravity field, parity anomaly results in a gravitational Chern-Simons term [23–26]. This leads to a quarter-quantized thermal Hall conductance, expressed as $\kappa_{\mathrm{H}} = \mathrm{sgn}(M)\frac{1}{4}\frac{\pi^2 k_{\mathrm{B}}^2}{3h}\mathcal{T}_0 = \mathrm{sgn}(M)\frac{1}{4}\kappa_0$, where $\kappa_0 = \frac{\pi^2 k_{\mathrm{B}}^2}{3h}\mathcal{T}_0$ is the quantum thermal conductance, $\mathcal{T}_0$ is the temperature, and M is the mass for the regulator [24,25]. To achieve parity anomaly in a Majorana system, a system with a single gapless Majorana cone is required. In time-reversal-invariant (TRI) topological superconductors (TSCs), each surface hosts a single Majorana cone [23,27,28]. A naive analogy is drawn to the case of semimagnetic 3D topological insulators (TIs) where breaking time reversal on one surface achieves parity anomaly in a Majorana system. However, the absence of bulk materials confirmed as TRI TSCs poses experimental challenges for all TRI-TSC-based approaches [23].

In this paper, we propose an approach to realize parity anomaly in a Majorana system without the need for TRI TSC bulk materials. By introducing superconducting pairing through proximity effects on a magnetic topological surface state, a massless Majorana fermion will emerge when the superconducting pairing gap matches the surface magnetization gap. Additionally, by constructing a system featuring only a single Majorana cone, we show that an $N = 1/2$ Majorana chiral edge current emerges on the boundary between a massless Majorana fermion and a massive Majorana fermion. Utilizing nonequilibrium Green's function (NEGF) calculations for a six-terminal Hall-bar system, we identity that the parity anomaly leads to a quarter-Hall thermal conductance plateau under the influence of dephasing. Finally, by mapping the system to a conductor-network model, we demonstrate the connection between the appearance of the $1/4$ Hall thermal conductance plateau and the presence of quarter-quantized chiral Majorana channels.

---

[*] Corresponding author: sunqf@pku.edu.cn

2469-9950/2024/109(19)/195408(9)

The paper is structured as follows. In Sec. II, by using a low-energy effective model, we provide a physical depiction of achieving a single gapless Majorana cone. Section III employs numerical methods to illustrate the existence of an $N = 1/2$ Majorana edge chiral current in the Majorana parity anomaly system. In Sec. IV, we calculate the $1/4$ Hall thermal conductance in the system under dephasing using NEGF. Besides, by solving a conductor-network model, we establish the relationship between $1/4$ Hall thermal conductance and the appearance of $1/4$ quantized chiral channels. The stability of the Hall thermal conductance under temperature variations is investigated in Sec. V. We address experimental implementation and conclude with a summary in Sec. VI. Additional computational details and supplementary figures are provided in Appendixes A to C.

II. SINGLE MASSLESS MAJORANA FERMION AND PARITY ANOMALY

First, starting from the low-energy model of the surface of the 3D TI, we present a physical picture for realizing a single gapless Majorana cone. The surface of the 3D TI hosts a single gapless Dirac cone, with low-energy effective Hamiltonian expressed as $H_{\rm surf}(k) = A(k_x s_x + k_y s_y)$ on the basis $(c_{\mathbf{k}\uparrow}, c_{\mathbf{k}\downarrow})$, where $s_{i=x,y,z}$ denotes Pauli matrices on the spin space and A is a parameter related to the Fermi velocity. A gapless Dirac cone can be interpreted as two gapless Majorana cones in the Bogoliubov–de Gennes representation [29,30]. Achieving parity anomaly of the Majorana system based on 2D topological surface states would be possible if there existed a method to selectively open the gap of one Majorana cone while keeping the other gap closed. Introducing both magnetization and superconductivity, the surface Hamiltonian in the Majorana basis Ψ_k is block-diagonalized into two components: $H_\pm = A(k_x s_x \pm k_y s_y) + (\Delta \pm M_A)s_z$. Here, Δ represents the superconducting pairing potential, and M_A signifies the surface magnetization. The Majorana basis Ψ_k is defined as $\Psi_{\mathbf{k}} = \frac{1}{\sqrt{2}}(c_{\mathbf{k}\uparrow} + c^\dagger_{-\mathbf{k}\downarrow}, c_{\mathbf{k}\downarrow} + c^\dagger_{-\mathbf{k}\uparrow}, -c_{\mathbf{k}\downarrow} + c^\dagger_{-\mathbf{k}\uparrow}, -c_{\mathbf{k}\uparrow} + c^\dagger_{-\mathbf{k}\downarrow})^T$, where $c^\dagger_{\mathbf{k}\uparrow/\downarrow}$ and $c_{\mathbf{k}\uparrow/\downarrow}$ are the creation and annihilation operators for electrons [30–32].

In this scenario, $H_\pm$ can be interpreted as 2D massive Majorana fermions with different chirality on the surface, characterized by masses $\Delta \pm M_A$. This model can be considered analogous to the Haldane model, which features massive Dirac fermions of opposite chirality in the K and K' valleys of graphene [18]. The mass term induces the opening of gaps in the Majorana cone $H_\pm$ [as illustrated in Fig. 1(a)], with the corresponding gap's Chern number given by $N_\pm = \frac{1}{2}{\rm sgn}(M_A \pm \Delta)$ [31]. For convenience in the following discussion, we consider $M_A > 0$ and $\Delta > 0$. When $\Delta < M_A$, both gaps in $H_\pm$ have Chern numbers of $1/2$, resulting in a total Chern number $N = N_+ + N_- = 1$. As Δ increases beyond M_A, accompanied by the gap closing and reopening of the Majorana cone corresponding to H_-, the Chern number in the corresponding gap changes from $1/2$ to $-1/2$, yielding a total Chern number $N = 0$. When $\Delta = M_A$, the Majorana cone corresponding to H_- becomes precisely gapless, giving rise to the coexistence of massless 2D Majorana fermions with massive 2D Majorana fermions on one surface, resulting in a total Chern number of $1/2$. Introducing an out-of-plane magnetization M_A on all surfaces of a 3D TI and a superconducting pairing potential Δ specifically on the top surface, where $\Delta = M_A$, results in a system featuring a single gapless Majorana cone [see Fig. 1(b)]. Drawing parallels with a system possessing a single gapless Dirac cone [22,33,34], a Majorana edge chiral current with $N = 1/2$ emerges on the boundary of the top surface due to the parity anomaly.

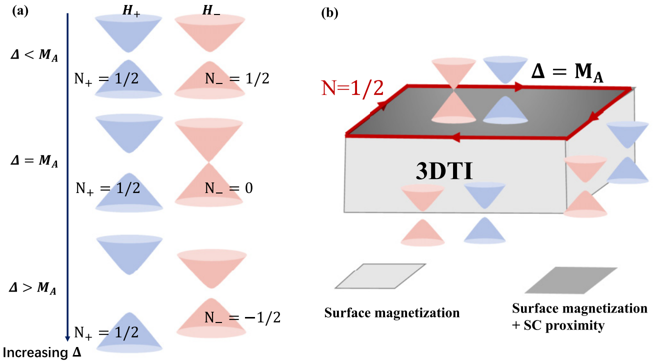

FIG. 1. (a) Schematic diagram of the changes in the two Majorana cones on the magnetic topological surface as the superconducting pairing potential Δ increases, with the Majorana cones corresponding to H_+ and H_- represented in blue and red, respectively. (b) Schematic diagram of the system with single gapless Majorana cone on the top surface, with red and blue cones representing Majorana cones corresponding to H_+ and H_-, respectively.

III. $N = 1/2$ MAJORANA EDGE CHIRAL CURRENT

Next, we use numerical methods to demonstrate the existence of the $N = 1/2$ Majorana edge chiral current. The Hamiltonian of a 3D TI in a cubic lattice is given by [35]

$$\mathcal{H}_{\rm TI} = (m - 6B)s_0\sigma_z + \sum_i (2Bs_0\sigma_z \cos k_i + As_i\sigma_x \sin k_i), \tag{1}$$

where m, B, and A are the model's parameters, and k_i is the momentum with $i = x, y, z$. s_i and σ_i are the Pauli matrices on the spin and orbital spaces. By choosing parameters $m = 1$ and $B = 0.6$, the 3D TI is placed in a nontrivial topological phase. Using Eq. (1), we establish a lattice model with open boundary conditions in the x and z directions while maintaining translational symmetry in the y direction. The widths in the x and z directions are denoted as L_x and L_z, respectively [see Fig. 2(a)]. Then, we introduce an out-of-plane magnetization M_A on all surfaces. Additionally, on the top surface, a superconducting pairing potential Δ arises through proximity to an s-wave superconductor. With $\Delta = M_A$, a gapless Majorana cone (shown in red) emerges on the top surface, along with a gapped Majorana cone featuring a gap of $4M_A$ [blue cone on the top surface of Fig. 2(a)]. The remaining surfaces exhibit two Majorana cones with gaps of $2M_A$ each. At the boundary of the top surface, a Majorana chiral edge current with $N = 1/2$ [depicted by red and blue arrows in Fig. 2(a)] appears, and we will delve into this phenomenon in the subsequent discussion.

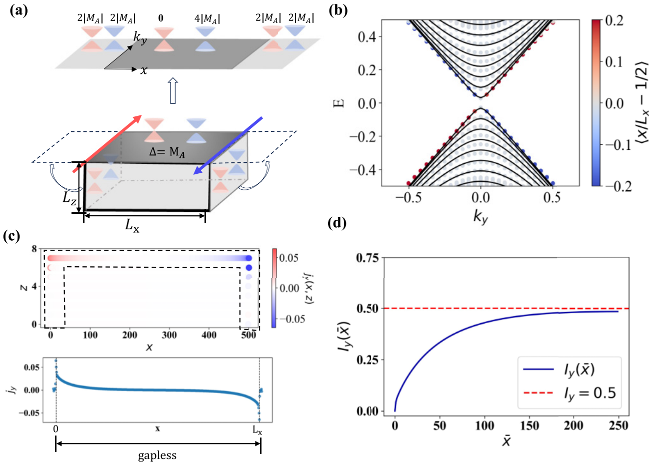

FIG. 2. (a) Schematic diagrams for the 3D TI (lower) and the unfolding of its surface into a quantum well (upper), with red and blue cones representing Majorana cones corresponding to H_+ and H_-, respectively. (b) The analytical results (black lines) and numerical results (scatter plot) of the model's band structure, with colors indicating the average displacement relative to the center for each Bloch state $\langle x/L_x - 1/2\rangle$. We set $L_x = 50$, $L_z = 5$ in the calculation. (c) The upper panel is the distribution of Majorana current density in the x-z plane. The lower panel describes the changes in surface current corresponding to the dashed black box in the upper panel. (d) The variation in Majorana current flux as the summation range $\bar{x}$ increases. In both (c) and (d), we have set $L_x = 500$, $L_z = 8$, and $\eta = 0.008$.

The surface of this model can be effectively unfolded into a quantum well model [upper subplot in Fig. 2(a)]. Due to the absence of coupling between the Majorana cones corresponding to H_+ (blue cone) and H_- (red cone), they can be treated independently. Since the Majorana cone associated with H_+ is gapped on all surfaces and exhibits no states in the energy window of interest (near $E = 0$), our focus can be directed toward the quantum well model formed by the red cone, with gapped Majorana cones at both ends and a gapless Majorana cone in the middle. To analyze the energy spectrum of this model, we can obtain analytical expressions by considering energy scales much smaller than the gap of the massive cones: $\varepsilon_n(k_y) = A\sqrt{k_y^2 + [\frac{\pi(n+1/2)}{L_x}]^2}$ $(n \in \mathbb{N})$ [33]. The finite-size effect leads to an energy gap inversely proportional to the width L_x. Figure 2(b) demonstrates good agreement between the numerical and analytical energy spectra, particularly in the low-energy region. We compute the average displacement relative to the center for each Bloch state: $\langle x/L_x - 1/2\rangle$, marked with colors in Fig. 2(b). States on the left (red) and right (blue) exhibit opposite velocities, indicating the chiral nature of the system. Furthermore, we calculate the distribution of Majorana current density at energy E in the x-z plane with $r = (x, z)$:

$$J_y(E, \boldsymbol{r}) = -\frac{e}{\pi h}\int_{-\pi}^{\pi} \mathrm{Im}\,\mathrm{Tr}\left[\frac{\partial H(k_y)}{\partial k_y} G^R_{k_y}(E, \boldsymbol{r}, \boldsymbol{r})\right] dk_y,$$

where $G^R_{k_y}(E, \mathbf{r}, \mathbf{r}')$ is the retarded Green's function for $H(k_y)$, which can be written as $G^R_{k_y}(E, \mathbf{r}, \mathbf{r}') = \langle \mathbf{r}|[E - H(k_y) + i\eta]^{-1}|\mathbf{r}'\rangle$. The upper panel in Fig. 2(c) shows the distribution of $J_y(E = 0)$ on the x-z interface. The opposite-directional current density exists at the left and right boundaries of the top surface, further confirming the chiral nature of the system. The current density exhibits distinct decay patterns in the gapless top surface region and the gap left and right regions, to better observe the decay trend of current density at the boundaries of the two regions (gap and gapless); see the lower panel in Fig. 2(c). The current density rapidly decays in the gap region, while it decreases slowly in the gapless region. As shown in Fig. 2(d), the Majorana current flux $I_y(\bar{x}) = \int_0^{L_z} dz \int_0^{\bar{x}} dx J_y(x, z)(\bar{x} < L_x/2)$ gradually converges to $1/2$ with increasing $\bar{x}$, demonstrating the presence of the $N = 1/2$ Majorana current. Furthermore, since a chiral Majorana fermion corresponds to half of a complex fermion and contributes half-quantized thermal Hall conductance, we can establish the relationship between Hall thermal conductance and Chern number N as $\kappa_{xy} = \frac{N}{2}\kappa_0$ [29,31,36]. Considering the Majorana edge current with $N = 1/2$ here, we can expect the exhibiting of a quarter-quantized Hall thermal conductance along with a quarter-quantized chiral heat channel. This will be demonstrated in Sec. IV.

IV. QUARTER-QUANTIZED THERMAL HALL CONDUCTANCE

Thermal transport is very useful for studying Majorana systems because it effectively avoids the situation where superconducting systems cannot couple with electric field [24,26,36,37]. In a 2D chiral topological system, the presence of 1D Majorana fermions at the edge contributes a half-integer thermal Hall effect to the system. Recently, the half-integer thermal Hall effect has been observed in the fractional quantum Hall system at $\upsilon = 5/2$ [38] and Kitaev material α-RuCl$_3$ [39]. Subsequently, we will illustrate the emergence of a quarter-quantized thermal Hall conductance in our system as a consequence of the parity anomaly.

Utilize the cubic lattice model introduced in Sec. III, employing open boundary conditions in the xyz direction, where $L_x = L_y = 110$ and $L_z = 5$. With the superconducting pairing potential Δ on the top surface equal to the surface magnetization M_A, a single gapless Majorana cone emerges on the top surface, resulting in a $1/4$ Hall thermal conductance in the system due to the parity anomaly. To investigate surface transport, we introduce a six-terminal Hall-bar device [see Fig. 3(a)], with ports I and IV designated as thermal flow ports, and ports II, III, V, and VI as temperature ports. The dephasing effect is simulated by introducing Büttiker virtual leads at each lattice point on the top surface [represented by red spheres in Fig. 3(b)] [40–42]. Utilizing the Landauer-Büttiker formula, the heat current flowing in the lead n at low temperatures can be expressed as [31,43,44]

$$Q_n = \sum_{m \neq n} (T_{mn}\mathcal{T}_n - T_{nm}\mathcal{T}_m)\kappa_0, \tag{2}$$

where $\mathcal{T}_m$ is the temperature in lead m, and $T_{nm}(E = 0) = T^{ee}_{nm}(E = 0) + T^{\mathrm{CAR}}_{nm}(E = 0)$. Here $T^{ee/\mathrm{CAR}}_{nm}(E = 0)$ denotes the transmission coefficient of electrons and the cross Andreev process with energy E from lead m to lead n, respectively. All

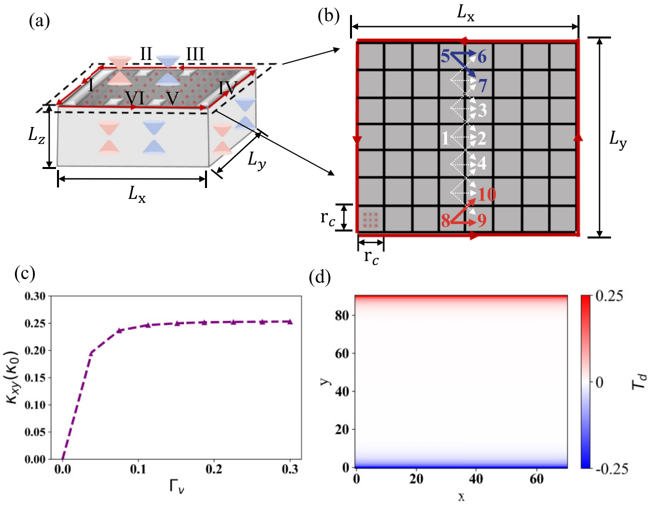

FIG. 3. (a) Illustration of a 3D TI with open boundary conditions in the x, y, and z directions, featuring ports attached to the top surface (highlighted in metallic shade). The red and blue cones correspond to the Majorana cones on the surface. Red balls here represent the virtual leads. (b) The red balls on the top surface in (a) are divided into black boxes, with each black box containing $r_c \times r_c$ red balls. (c) Variation of thermal Hall conductance with the strength of the dephasing strength Γ_v. (d) The spatial distribution of the difference in transmission coefficients T_d with $\Gamma_v = 0.2$. Here, we set $M_A = 0.5$ and $\Delta = 0.5$.

these transport coefficients are calculated as [45] $T_{nm}(E) = \mathrm{Tr}[\Gamma_n^e \mathbf{G}^R \Gamma_m^e \mathbf{G}^A]$, $T_{nm}^{\mathrm{CAR}}(E) = \mathrm{Tr}[\Gamma_n^e \mathbf{G}^R \Gamma_m^h \mathbf{G}^A]$, where Γ_n is the linewidth function of the nth port, which, in the wideband approximation, is a constant, and $\mathbf{G}^R(E) = [\mathbf{G}^A]^\dagger = [(E + \mathbf{i}\eta)\mathbf{I} - \mathbf{H} - \sum_n \Sigma_n^R]^{-1}$. The self-energy term is $\Sigma_n^R = -\frac{\mathbf{i}}{2}\Gamma_n$. For virtual leads, the self-energy $\Sigma_n^R = -\frac{\mathbf{i}}{2}\Gamma_v$, where Γ_v is the decoherence strength [41].

When there is a heat current Q_x from lead I to lead IV, by solving Eq. (2), the Hall thermal resistance and longitudinal thermal resistance are obtained as $R_{xy} = \frac{\mathcal{T}_{II} - \mathcal{T}_{VI}}{Q_x}$ and $R_{xx} = \frac{\mathcal{T}_{II} - \mathcal{T}_{III}}{Q_x}$, respectively. As only the top surface is gapless, the heat current can only occur on the top surface. The thermal resistivities satisfy $\rho_{xy} = R_{xy}$ and $\rho_{xx} = \frac{R_{xx}}{L_x/L_y}$. The thermal Hall conductance of the system can be obtained through $\kappa_{xy} = \frac{\rho_{xy}}{\rho_{xy}^2 + \rho_{xx}^2}$.

Figure 3(c) illustrates the variation of Hall thermal conductance κ_{xy} with increasing dephasing strength Γ_v. At sufficiently large dephasing strength, the Hall thermal conductance converges to $1/4$, with units the quantum thermal conductance κ_0. There are two main reasons to consider the dephasing effect here. First, in real experiments, the sizes of samples often reach the order of several hundred micrometers, far surpassing the decoherence length; it is necessary to take the dephasing effect into consideration [21]. Second, the chiral transport channels can manifest when the dephasing strength is large enough [14].

Next, we provide an explanation for the origin of the quarter-quantized thermal Hall effect under dephasing. The thermal Hall conductance is closely connected to the chiral transport channels. Chiral channels break spatial inversion symmetry. For instance, considering the transmission probability between site a and site b, if there is a chiral channel between them, it implies $T_{ab} \neq T_{ba}$, where T_{ab} (T_{ba}) represents the transmission probability from a to b (b to a). In contrast to the chiral p-wave superconductor [28] where only the 1D chiral Majorana edge mode exists within the energy gap, here the gapless Majorana surface state on the top surface serves as a 2D thermal conductor. This involves contributions from both isotropic 2D bulk (top surface) transport and 1D boundary chiral transport. The calculation of the difference in transmission probabilities cancels the isotropic contributions, allowing the extraction of boundary chiral transport. To observe the spatial distribution of chiral channels, the system should be partitioned into sufficiently large blocks, ensuring that decoherence exists between these blocks due to their size being much larger than the coherence length. The calculation of the difference in transmission probabilities between blocks provides insight into the spatial distribution of chiral transport channels. As the transmission probability T_{nm} between lead n and lead m decreases sharply with the increasing distance r_{nm} (see Fig. 5 in Appendix A), the critical length can be defined as $T_{nm} = 0.001 T_{\mathrm{neigb}}$ [41], where T_{neigb} is defined as the sum of the transmission coefficient of electrons and the cross Andreev process between the nearest neighboring leads. We can use black boxes to demarcate these regions of size $r_c \times r_c$ [Fig. 3(b)]. Due to r_c being much larger than the phase coherent length [41], the transmission between two adjacent black boxes becomes incoherent. We can define the difference of transmission coefficients between two black boxes, denoted as $T_d(x, y) = T_{ba} - T_{ab}$, where (x, y) represents the spatial coordinates of the lower right corner site in box a. Here, $T_{ab} = \sum_{n \in a, m \in b} T_{nm}$ represents the transmission probability from box a to box b. Figure 3(d) illustrates the spatial distribution of T_d, revealing a transmission probability difference along the upper and lower boundaries: $T_d = \pm 1/4 = \pm t_{\mathrm{chiral}}$. This implies the existence of quarter-quantized heat chiral channels along the upper and lower boundaries, serving as the origin of the quarter-quantized thermal Hall effect in Fig. 3(c).

To further illustrate the connection between the quarter-quantized chiral channels and the quarter-quantized thermal Hall effect here, we partition the top surface of the system (where single massless Majorana fermion exists) into blocks of size $r_c \times r_c$ [black box in Fig. 3(b)]. Due to the decoherence between these blocks, the system can be effectively represented as a conductor-network model that describes the transport in classical metals. Through analytical solutions of the network model (see Appendix A), we establish the relationship between the thermal Hall conductance κ_{xy} and the difference in transmission probability at the edge t_{chiral}:

$$\kappa_{xy} = \kappa_0 \left[1 + \frac{r_c \alpha t_{\mathrm{chiral}} + t_n^2}{t_{\mathrm{chiral}}^2 + t_n^2} \frac{1}{L_y} \right] t_{\mathrm{chiral}}.$$

Here, $t_n = \frac{t_{13} + t_{12} + t_{14}}{r_c}$, $\alpha = t_{56} + t_{57} + t_{89} + t_{810} - 2t_n$, where $t_{ij} = \sum_{n \in i, m \in j} T_{nm} x_{nm}$ [see Fig. 3(b)], $x_{nm} = x_n - x_m$, and $x_{n(m)}$ represent the x coordinate of lead $n(m)$. The width of the system L_y correlates with the quarter-quantized thermal Hall conductance. As L_y approaches infinity, $\kappa_{xy} = t_{\mathrm{chiral}} \kappa_0$.

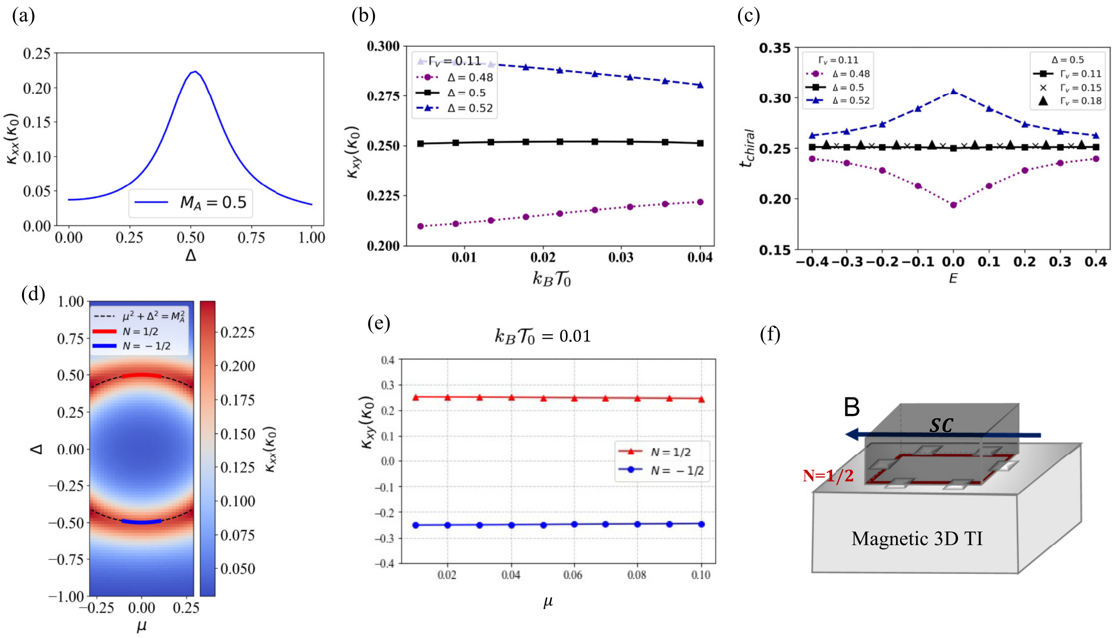

FIG. 4. (a) For $\mu = 0$, the longitudinal thermal conductance κ_{xx} varies with the surface superconducting pairing potential Δ. (b) The Hall thermal conductance changes with the background temperature $k_B\mathcal{T}_0$ for different Δ. (c) The transmission probability difference t_{chiral} varies with energy E for different Δ and different dephasing strength Γ_v. (d) Longitudinal thermal conductance κ_{xx} varying with Δ and μ, with the dashed line representing the theoretically predicted phase transition curve. (e) Thermal Hall conductance κ_{xy} on the red and blue curves in graph (d), with a temperature of $k_B\mathcal{T}_0 = 0.01$. (f) Experiment setup to realizing parity anomaly in gapless Majorana surface state through a magnetic 3D TI-superconductor heterostructure. The superconductor (deep gray) is overlaid on the surface of the magnetic 3D TI. By adjusting the superconducting pairing potential by a magnetic field, when gapless Majorana surface state appears, the boundary exhibits $N = 1/2$ Majorana edge chiral states (represented by red lines). A quarter of the thermal Hall effect can be measured through a six-port Hall-bar system (silver). In the calculations, $L_x = 50$, $L_y = 50$, and $L_z = 5$, with $\Gamma_v = 0.15$ adopted in (a), (d), and (e), while $L_x = 70$, $L_y = 70$, and $L_z = 5$ in (b) and (c).

V. TEMPERATURE DEPENDENCE OF THERMAL HALL CONDUCTANCE

Our model relies on fine-tuning to align the superconducting pairing potential Δ with the surface magnetization M_A, representing critical points in the phase transition. However, the phase transition point here exhibits distinctive features that can be captured in experiments. Since the realization of the gapless Majorana surface state is essentially a phase transition point between $N = 0$ and $N = 1$ [31], the states before and after are either insulating or 1D thermal conductors. At the phase transition point, where the system transforms into a 2D thermal conductor, a distinctive peak emerges in the longitudinal thermal conductance κ_{xx}. Figure 4(a) depicts the variation of κ_{xx} calculated using the Landauer-Büttiker formula with changing superconducting pairing potential Δ. A pronounced peak appears when $\Delta = M_A$. In Fig. 4(b), the temperature-dependent behavior of the Hall thermal conductance κ_{xy} for different Δ is presented (for more details see Appendix B). Here, we consider $k_BT \ll \Delta$, allowing us to neglect the influence of temperature on Δ, which can be solely controlled by the magnetic field. Notably, for the case of $\Delta = M_A$, κ_{xy} exhibits a quantized plateau under temperature variations. However, as Δ deviates from M_A [e.g., $\Delta = 1.04M_A$ and $0.96M_A$; dashed and dotted lines in Fig. 4(b)], not only does κ_{xy} lose its quarter quantization, but the plateau disappears as well.

The Hall thermal conductance at finite temperature depends on the all transport channels for an energy scale of a few $k_B\mathcal{T}_0$ near the Fermi level. This relationship is expressed as $\kappa_{xy}(\mathcal{T}_0) = \frac{1}{h}\int t_{\text{chiral}}(E)E\frac{\partial f_0}{\partial \mathcal{T}}dE$, where $f_0(E)=1/[e^{E/k_B\mathcal{T}_0}+1]$ is the Fermi distribution (see Appendix B for details). When $\Delta = M_A$, a single gapless Majorana cone exists on the surface. In this case, the chiral transmission coefficient, $t_{\text{chiral}}(E)$, which directly determines the thermal Hall conductance κ_{xy}, remains energy independent and is equal to $1/4$ [Fig. 4(c)]. Consequently, the $1/4$ thermal Hall plateau persists under temperature variations [Fig. 4(b)], providing evidence for the existence of a single gapless Majorana cone. It is important to note that the role of dephasing here is to reduce the coherence length of the system. Even if the dephasing strength varies, as long as the coherence length of the system is much smaller than the system width L_y, t_{chiral} remains energy independent and stays close to $1/4$ [see Fig. 4(c)]. When Δ deviates from M_A (e.g., $\Delta = 1.04M_A$ and $0.96M_A$), $t_{\text{chiral}}(E)$ gradually becomes energy dependent [Fig. 4(c)], leading to κ_{xy} depending on the temperature $\mathcal{T}_0$ also [Fig. 4(b)].

The preceding analysis is based on the result with chemical potential $\mu = 0$, representing a specific case where electrons precisely fill the Dirac point. While experimental means exist to adjust μ, achieving the exact filling of electrons at the Dirac point remains challenging. To better align with experimental conditions, we consider the influence of μ. In the case of a nonzero chemical potential, the phase transition point satisfies ${M_A}^2 = \Delta^2 + \mu^2$. Figure 4(d) illustrates the longitudinal thermal conductance κ_{xx} varying with Δ and μ at the fixed M_A. The presence of the 2D thermal conductor at the phase transition point results in a peak in κ_{xx}. We extract two intervals along the phase transition curve to compute the corresponding Hall thermal conductance κ_{xy} [indicated by red and blue dashed lines in Fig. 4(d)]. κ_{xy} maintains a quarter quantization with variation of μ, as shown in Fig. 4(e). Theoretically, the chemical potential μ induces coupling between the two Majorana cones (see Appendix C for details). However, when $\mu \ll M_A$, the gapless Majorana surface states on the top surface can be well preserved, so the quarter-quantized Hall thermal conductance well survives still.

VI. DISCUSSION AND CONCLUSION

Realizing parity anomaly in the Majorana system relies crucially on the interplay between the topological surface state and superconductivity as well as magnetism. There are two approaches to achieving the coexistence of 2D topological surface states, superconductivity and magnetism. One relies on the magnetic TI with surface-proximity-induced superconductivity, naturally hosting topological surface states with magnetism. Similar experimental configurations have been experimentally realized very recently [46–48]. The experimental setup involves inducing s-wave superconductivity on the surface of a magnetic 3D TI, and arranging six-terminal Hall-bar measurements along the superconducting boundary to study the thermal transport properties of the surface [see Fig. 4(f)]. By adjusting the magnetic field to tune the superconducting gap (Δ), a peak in κ_{xx} will be observed at the phase transition point. When chemical potential μ nears the Dirac point, the gapless Majorana surface state emerges at the phase transition point, accompanied by a temperature-dependent quarter-quantized Hall thermal platform at low temperatures. Another approach is topological iron-based superconductors. Coexistence of superconductivity and topological surface states is observed in materials like $\mathrm{FeTe_{0.55}Se_{0.45}}$ [49,50], with experiments confirming 0D Majorana states on the vortex of the surface [51–54]. Here, we propose that by coupling a magnetic atomic layer to the surface, providing surface magnetism, 2D Majorana surface states can be realized in such materials. The Fermi level of $\mathrm{FeTe_{0.55}Se_{0.45}}$ is very close to the Dirac point [51]. Simultaneously, the superconducting gap on the surface is 1.8 meV [51], a magnitude comparable to the magnetic gap provided by magnetic proximity effects [55], which enhances the feasibility of the experiment.

In summary, we present an approach based on 2D topological surface state to achieve 2D Majorana surface states. We analytically and numerically demonstrate that a system with a single massless Majorana possesses an $N = 1/2$ Majorana edge current and a quarter-quantized Hall thermal conductance. This signifies the presence of a parity anomaly in the system, resembling the superconducting version of a quantum anomalous semimetal. By mapping the system to a network model, we elucidate that the appearance of the $1/4$ thermal Hall plateau under the dephasing effect originates from the $1/4$ chiral channels at the boundary. Furthermore, we verify κ_{xy} robustly quarter quantized within a range of background temperature $\mathcal{T}_0$. We also identify the magnetic topological insulator and the topological iron-based superconductor $\mathrm{FeTe_{0.55}Se_{0.45}}$ as potential platforms for realizing Majorana surface states. Our study provides a framework for the experimental realization of parity anomaly in the Majorana system.

ACKNOWLEDGMENTS

Y.-H.W. is grateful to Hu-Mian Zhou, Qing Yan, and Ludan Zhang for fruitful discussions. This work was financially supported by the National Natural Science Foundation of China (Grants No. 12374034 and No. 11921005), the Innovation Program for Quantum Science and Technology (Grant No. 2021ZD0302403), and the Strategic Priority Research Program of the Chinese Academy of Sciences (Grant No. XDB28000000). We also acknowledge the High-Performance Computing Platform of Peking University for providing computational resources.

APPENDIX A: LANDAUER-BÜTTIKER FORMULA AND THERMAL HALL CONDUCTANCE

We consider a surface with dimensions $L_x \times L_y$ hosting a gapless Majorana surface state. This surface is partitioned into a system of blocks, each with dimensions $r_c \times r_c$ [see Fig. 3(b)]. As the distance $r_{nm} > r_c$, the transmittance probability T_{nm} between lead n and m becomes nearly zero (see Fig. 5), resulting in nonzero transmittance only between neighboring blocks [indicated by arrows in Fig. 3(b)]. We focus on the total heat flow Q_x in the horizontal direction within the central region of the system,

$$\begin{aligned}
Q_x &= \sum_{n\in\text{left},m\in\text{right}} Q_{nm} = \sum_{n\in\text{left},m\in\text{right}} (T_{nm}\mathcal{T}_m - T_{mn}\mathcal{T}_n)\kappa_0 \\
&= \sum_{n\in\text{left},m\in\text{right}} T_{nm}(\mathcal{T}_m - \mathcal{T}_n)\kappa_0 \\
&\quad + \sum_{n\in\text{left},m\in\text{right}} (T_{nm} - T_{mn})\mathcal{T}_n\kappa_0 \\
&= \sum_{n\in\text{left},m\in\text{right}} T_{nm}(x_{nm}\nabla\mathcal{T}_x + y_{nm}\nabla\mathcal{T}_y)\kappa_0 \\
&\quad + \sum_{n\in 6,m\in 5} (T_{nm} - T_{mn})\mathcal{T}_n\kappa_0 + \sum_{n\in 9,m\in 8} (T_{nm} - T_{mn})\mathcal{T}_n\kappa_0.
\end{aligned} \tag{A1}$$

Here, $x_{nm} = x_n - x_m$ and $y_{nm} = y_n - y_m$, where $x_{n(m)}$ and $y_{n(m)}$ represent the x coordinate and y coordinate of lead $n(m)$. We assume that in the central region of the system, where steady state is reached, the temperature gradient is constant. T_{nm} denotes the transmittance probability from lead m to lead n, with the assumption that T_{nm} has translational symmetry except at the boundaries.

The first term of Eq. (A1), $\sum_{n\in\text{left},m\in\text{right}} T_{nm}(x_{nm}\nabla\mathcal{T}_x + y_{nm}\nabla\mathcal{T}_y)\kappa_0$, can be categorized into two types: $L_y/r_c - 2$ contributions from the bulk [indicated by white dashed arrows in Fig. 3(b)] and two contributions from the boundaries [indicated by red and blue arrows in Fig. 3(b)]. The contribution from the bulk can be expressed as $[(L_y/r_c) - 2](t_{13} + t_{12} +$

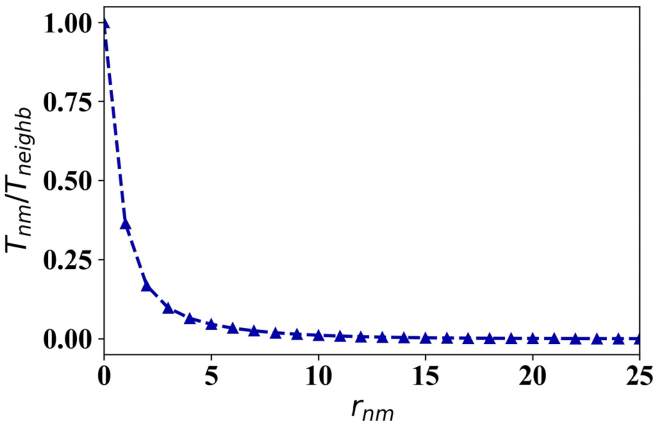

FIG. 5. $T_{nm}/T_{\rm neighb}$ vs the distance r_{nm} with $\Gamma_v = 0.2$.

$t_{14})\nabla\mathcal{T}_x$, where $t_{ij} = \sum_{n\in i, m\in j} T_{nm}x_{nm}$ [see Fig. 3(b)]. Note that terms related to y_{nm} disappear due to $T_{13}y_{13} + T_{14}y_{14} = 0$. The contribution from the edges can be written as $(t_{56} + t_{57} + t_{89} + t_{810})\nabla\mathcal{T}_x$. Therefore, Eq. (A1) can be expressed as

$$\begin{aligned} Q_x &= \bigg[\bigg(\frac{L_y}{r_c} - 2\bigg)(t_{13} + t_{12} + t_{14})\nabla\mathcal{T}_x + (t_{56} + t_{57} \\ &\quad + t_{89} + t_{810})\nabla\mathcal{T}_x + t_{\rm chiral}\mathcal{T}_{\rm up} - t_{\rm chiral}\mathcal{T}_{\rm low}\bigg]\kappa_0 \\ &= [(L_y - 2r_c)t_n\nabla\mathcal{T}_x + r_c\alpha\nabla\mathcal{T}_x + t_{\rm chiral}\mathcal{T}_{\rm up} - t_{\rm chiral}\mathcal{T}_{\rm low}]\kappa_0 \\ &= [\big(t_nL_y + r_c\alpha\big)\nabla\mathcal{T}_x + t_{\rm chiral}(\mathcal{T}_{\rm up} - \mathcal{T}_{\rm low})]\kappa_0 \\ &= [(t_nL_y + r_c\alpha)\nabla\mathcal{T}_x + t_{\rm chiral}\nabla\mathcal{T}_yL_y]\kappa_0. \end{aligned}$$

The expression for t_n is defined as $t_n = \frac{t_{13}+t_{12}+t_{14}}{r_c}$, and $\alpha = t_{56} + t_{57} + t_{89} + t_{810} - 2t_n$. Here, $\mathcal{T}_{\rm up/down}$ represents the temperatures at the upper and lower boundaries, satisfying $\mathcal{T}_{\rm up} - \mathcal{T}_{\rm low} = \nabla\mathcal{T}_y \cdot L_y$. Similarly, the heat flow in the y (vertical) direction is given by

$$Q_y = [(t_nL_x + r_c\alpha)\nabla\mathcal{T}_y - t_{\rm chiral}\nabla\mathcal{T}_xL_x]\kappa_0.$$

Considering $Q_y = 0$ and $L_x \gg 0$, we obtain $t_n\nabla\mathcal{T}_y = t_{\rm chiral}\nabla\mathcal{T}_x$. Due to $\rho_{xx} = L_x\nabla\mathcal{T}_x/Q_x$ and $\rho_{xy} = L_y\nabla\mathcal{T}_y/Q_x$, the expression for κ_{xy} can be derived as

$$\begin{aligned} \kappa_{xy} &= \frac{\rho_{xy}}{\rho_{xy}^2 + \rho_{xx}^2} \\ &= \bigg[1 + \frac{r_c\alpha t_{\rm chiral} + t_n^2}{t_{\rm chiral}^2 + t_n^2}\frac{1}{L_y}\bigg]t_{\rm chiral}\kappa_0. \end{aligned}$$

APPENDIX B: HALL THERMAL CONDUCTANCE WITH FINITE TEMPERATURE

In this Appendix, we will derive the Hall thermal conductance at finite temperature. We start from the nonzero-temperature Landauer-Büttiker formula:

$$Q_n = \sum_m \widetilde{T}_{nm}(\mathcal{T}_n - \mathcal{T}_m)\kappa_0,$$

where $\widetilde{T}_{nm} = \frac{3}{\pi^2k_{\rm B}^2\mathcal{T}_0}\int[T_{nm}(E) + T_{nm}^{\rm CAR}(E)]E\frac{\partial f_0}{\partial\mathcal{T}}dE$. The finite temperature modifies the transmission probability $T_{nm}(E)$ to $\widetilde{T}_{nm}$, introducing contributions from different energy transmissions. With the same mathematical structure, following the method in Appendix A, we obtain the total heat flows in the horizontal (x) and vertical directions as $Q_x = [(\widetilde{t}_nL_y + \widetilde{\alpha})\nabla\mathcal{T}_x + \widetilde{t}_{\rm chiral}\nabla\mathcal{T}_yL_y]\kappa_0$, $Q_y = [(\widetilde{t}_nL_x + \widetilde{\alpha})\nabla\mathcal{T}_y - \widetilde{t}_{\rm chiral}\nabla\mathcal{T}_xL_x]\kappa_0$. Here, $\widetilde{t}_n(\mathcal{T}_0) = \frac{3}{\pi^2k_{\rm B}^2\mathcal{T}_0}\int t_n(E)E\frac{\partial f_0}{\partial\mathcal{T}}dE$, $\widetilde{t}_{\rm chiral}(\mathcal{T}_0) = \frac{3}{\pi^2k_{\rm B}^2\mathcal{T}_0}\int t_{\rm chiral}(E)E\frac{\partial f_0}{\partial\mathcal{T}}dE$, and $\widetilde{\alpha} = \frac{3}{\pi^2k_{\rm B}^2\mathcal{T}_0}\int\alpha(E)r_cE\frac{\partial f_0}{\partial\mathcal{T}}dE$. The Hall thermal conductance can be written as

$$\kappa_{xy}(\mathcal{T}_0) = \kappa_0\bigg[1 + \frac{\widetilde{\alpha}\widetilde{t}_{\rm chiral} + \widetilde{t}_n^2}{\widetilde{t}_{\rm chiral}^2 + \widetilde{t}_n^2}\frac{1}{L_y}\bigg]\widetilde{t}_{\rm chiral}.$$

Considering $L_y \gg 0$, the expression simplifies to

$$\kappa_{xy}(\mathcal{T}_0) = \widetilde{t}_{\rm chiral}\kappa_0 = \frac{1}{h}\int t_{\rm chiral}(E)E\frac{\partial f_0}{\partial\mathcal{T}}dE.$$

APPENDIX C: MAJORANA SURFACE STATE WITH THE FINITE CHEMISTRY POTENTIAL

When considering the chemical potential μ, the critical point satisfies $M_A^2 = \Delta^2 + \mu^2$ [31]. The Hamiltonian with Majorana basis $\Psi_{\mathbf{k}} = \frac{1}{\sqrt{2}}(c_{\mathbf{k}\uparrow} + c_{-\mathbf{k}\downarrow}^\dagger, c_{\mathbf{k}\downarrow} + c_{-\mathbf{k}\uparrow}^\dagger, -c_{\mathbf{k}\downarrow} + c_{-\mathbf{k}\uparrow}^\dagger, -c_{\mathbf{k}\uparrow} + c_{-\mathbf{k}\downarrow}^\dagger)^T$ can be written as

$$\begin{aligned} H &= \begin{pmatrix} \Delta + M_A & k_x - ik_y & 0 & -\mu \\ k_x + ik_y & -\Delta - M_A & -\mu & 0 \\ 0 & -\mu & \Delta - M_A & k_x + ik_y \\ -\mu & 0 & k_x - ik_y & M_A - \Delta \end{pmatrix} \\ &= \begin{pmatrix} H_+(k) & -\mu\sigma_x \\ -\mu\sigma_x & H_-(k) \end{pmatrix}. \end{aligned}$$

The chemical potential μ induces coupling between the two Majorana cones and simultaneously opens gaps in both cones, with gap sizes of $2|\sqrt{M_A^2 - \mu^2} + M_A|$ for $H_+(k)$ and $2|\sqrt{M_A^2 - \mu^2} - M_A|$ for $H_-(k)$. Next, we demonstrate that the Majorana surface state exists when $\mu \ll M_A$. At $\mu \ll M_A$, $H_-(k)$ can be written as

$$\begin{aligned} H_-(k) &= k_x\sigma_x - k_y\sigma_y + \big(\sqrt{M_A^2 - \mu^2} - M_A\big)\sigma_z \\ &\approx k_x\sigma_x - k_y\sigma_y - \frac{M_A}{2}\bigg(\frac{\mu}{M_A}\bigg)^2\sigma_z. \end{aligned}$$

When $\mu \ll M_A$, the gap can be approximated as a second-order small quantity with respect to $\frac{\mu}{M_A}$. Simultaneously, μ introduces coupling between H_+ and H_-, and the mass term of H_+ affects H_- through this coupling. Let $M_+ = \sqrt{M_A^2 - \mu^2} + M_A$. Considering the mass term of H_+ and its self-energy correction to H_-, the expression is as follows:

$$\begin{aligned} \Sigma(E) &= -\mu\sigma_x\frac{1}{E - M_+\sigma_z}(-\mu\sigma_x) \\ &= \frac{\mu^2M_+}{-E^2 + M_+^2}\sigma_z - \frac{\mu^2E}{-E^2 + M_+^2}\sigma_0. \end{aligned}$$

Since $M_+ > M_A$, $\frac{\mu}{M_+}$ is also a small quantity. Therefore, the mass term correction introduced by H_+ to H_- is also a second-order small quantity. In summary, when $\mu \ll M_A$, the gapless Majorana Dirac cone can exist. In experiments, where M_A is typically 10 meV [56,57], it is possible to manipulate μ within the range of $0.1M_A$ by tuning the chemical potential.

[1] S. Murakami, New J. Phys. **9**, 356 (2007).
[2] N. P. Armitage, E. J. Mele, and A. Vishwanath, Rev. Mod. Phys. **90**, 015001 (2018).
[3] B.-J. Yang and N. Nagaosa, Nat. Commun. **5**, 4898 (2014).
[4] A. N. Redlich, Phys. Rev. Lett. **52**, 18 (1984).
[5] A. N. Redlich, Phys. Rev. D **29**, 2366 (1984).
[6] G. W. Semenoff, Phys. Rev. Lett. **53**, 2449 (1984).
[7] J. Böttcher, C. Tutschku, L. W. Molenkamp, and E. M. Hankiewicz, Phys. Rev. Lett. **123**, 226602 (2019).
[8] C.-Z. Chang, J. Zhang, X. Feng, J. Shen, Z. Zhang, M. Guo, K. Li, Y. Ou, P. Wei, L.-L. Wang, Z.-Q. Ji, Y. Feng, S. Ji, X. Chen, J. Jia, X. Dai, Z. Fang, S.-C. Zhang, K. He, Y. Wang *et al.*, Science **340**, 167 (2013).
[9] S. Zhang, L. Pi, R. Wang, G. Yu, X.-C. Pan, Z. Wei, J. Zhang, C. Xi, Z. Bai, F. Fei, M. Wang, J. Liao, Y. Li, X. Wang, F. Song, Y. Zhang, B. Wang, D. Xing, and G. Wang, Nat. Commun. **8**, 977 (2017).
[10] J. W. McIver, B. Schulte, F.-U. Stein, T. Matsuyama, G. Jotzu, G. Meier, and A. Cavalleri, Nat. Phys. **16**, 38 (2020).
[11] L. Lu, Nat. Phys. **14**, 875 (2018).
[12] T. Ozawa, H. M. Price, A. Amo, N. Goldman, M. Hafezi, L. Lu, M. C. Rechtsman, D. Schuster, J. Simon, O. Zilberberg, and I. Carusotto, Rev. Mod. Phys. **91**, 015006 (2019).
[13] G. Jotzu, M. Messer, R. Desbuquois, M. Lebrat, T. Uehlinger, D. Greif, and T. Esslinger, Nature (London) **515**, 237 (2014).
[14] H. Zhou, H. Li, D.-H. Xu, C.-Z. Chen, Q.-F. Sun, and X. C. Xie, Phys. Rev. Lett. **129**, 096601 (2022).
[15] Y. Xu, I. Miotkowski, C. Liu, J. Tian, H. Nam, N. Alidoust, J. Hu, C.-K. Shih, M. Z. Hasan, and Y. P. Chen, Nat. Phys. **10**, 956 (2014).
[16] Y. Tokura, K. Yasuda, and A. Tsukazaki, Nat. Rev. Phys. **1**, 126 (2019).
[17] Z. Ning, X. Ding, D.-H. Xu, and R. Wang, Phys. Rev. B **108**, L041104 (2023).
[18] F. D. M. Haldane, Phys. Rev. Lett. **61**, 2015 (1988).
[19] M. F. Lapa, Phys. Rev. B **99**, 235144 (2019).
[20] A. A. Burkov, Phys. Rev. B **99**, 035124 (2019).
[21] M. Mogi, Y. Okamura, M. Kawamura, R. Yoshimi, K. Yasuda, A. Tsukazaki, K. S. Takahashi, T. Morimoto, N. Nagaosa, M. Kawasaki, Y. Takahashi, and Y. Tokura, Nat. Phys. **18**, 390 (2022).
[22] B. Fu, J.-Y. Zou, Z.-A. Hu, H.-W. Wang, and S.-Q. Shen, npj Quantum Mater. **7**, 94 (2022).
[23] M. Sato and S. Fujimoto, J. Phys. Soc. Jpn. **85**, 072001 (2016).
[24] A. Furusaki, N. Nagaosa, K. Nomura, S. Ryu, and T. Takayanagi, C. R. Phys. **14**, 871 (2013).
[25] A. Sekine and K. Nomura, J. Appl. Phys. **129**, 141101 (2021).
[26] Z. Wang, X.-L. Qi, and S.-C. Zhang, Phys. Rev. B **84**, 014527 (2011).
[27] X.-L. Qi, T. L. Hughes, S. Raghu, and S.-C. Zhang, Phys. Rev. Lett. **102**, 187001 (2009).
[28] M. Sato and Y. Ando, Rep. Prog. Phys. **80**, 076501 (2017).
[29] S. B. Chung and S.-C. Zhang, Phys. Rev. Lett. **103**, 235301 (2009).
[30] X.-L. Qi and S.-C. Zhang, Rev. Mod. Phys. **83**, 1057 (2011).
[31] Q. Yan, H. Li, J. Zeng, Q.-F. Sun, and X. C. Xie, Commun. Phys. **4**, 239 (2021).
[32] X.-L. Qi, T. L. Hughes, and S.-C. Zhang, Phys. Rev. B **82**, 184516 (2010).
[33] J.-Y. Zou, B. Fu, H.-W. Wang, Z.-A. Hu, and S.-Q. Shen, Phys. Rev. B **105**, L201106 (2022).
[34] M. Gong, H. Liu, H. Jiang, C.-Z. Chen, and X.-C. Xie, Natl. Sci. Rev. **10**, nwad025 (2023).
[35] Y.-H. Wan and Q.-F. Sun, Phys. Rev. B **109**, 045418 (2024).
[36] N.-X. Yang, Q. Yan, and Q.-F. Sun, Phys. Rev. B **105**, 125414 (2022).
[37] W. Tang, X. C. Xie, L. Wang, and H.-H. Tu, Phys. Rev. B **100**, 155112 (2019).
[38] M. Banerjee, M. Heiblum, V. Umansky, D. E. Feldman, Y. Oreg, and A. Stern, Nature (London) **559**, 205 (2018).
[39] Y. Kasahara, T. Ohnishi, Y. Mizukami, O. Tanaka, S. Ma, K. Sugii, N. Kurita, H. Tanaka, J. Nasu, Y. Motome, T. Shibauchi, and Y. Matsuda, Nature (London) **559**, 227 (2018).
[40] M. Büttiker, Phys. Rev. Lett. **57**, 1761 (1986).
[41] Y. Xing, Q.-f. Sun, and J. Wang, Phys. Rev. B **77**, 115346 (2008).
[42] M. Buttiker, IBM J. Res. Dev. **32**, 317 (1988).
[43] W. Long, H. Zhang, and Q.-f. Sun, Phys. Rev. B **84**, 075416 (2011).
[44] C. J. Lambert, V. C. Hui, and S. J. Robinson, J. Phys.: Condens. Matter **5**, 4187 (1993).
[45] Q. Yan, Y.-F. Zhou, and Q.-F. Sun, Phys. Rev. B **100**, 235407 (2019).
[46] H. Yi, Y.-F. Zhao, Y.-T. Chan, J. Cai, R. Mei, X. Wu, Z.-J. Yan, L.-J. Zhou, R. Zhang, Z. Wang, S. Paolini, R. Xiao, K. Wang, A. R. Richardella, J. Singleton, L. E. Winter, T. Prokscha, Z. Salman, A. Suter, P. P. Balakrishnan *et al.*, Science **383**, 634 (2024).
[47] W.-Z. Xu, C.-G. Chu, Z.-C. Pan, J.-J. Chen, A.-Q. Wang, Z.-B. Tan, P.-F. Zhu, X.-G. Ye, D.-P. Yu, and Z.-M. Liao, Phys. Rev. B **105**, 184515 (2022).
[48] J. Chen, W. Xu, Z. Tan, Z. Pan, P. Zhu, Z.-M. Liao, and D. Yu, Nano Lett. **22**, 6484 (2022).
[49] P. Zhang, K. Yaji, T. Hashimoto, Y. Ota, T. Kondo, K. Okazaki, Z. Wang, J. Wen, G. D. Gu, H. Ding, and S. Shin, Science **360**, 182 (2018).
[50] P. Zhang, Z. Wang, X. Wu, K. Yaji, Y. Ishida, Y. Kohama, G. Dai, Y. Sun, C. Bareille, K. Kuroda, T. Kondo, K. Okazaki, K. Kindo, X. Wang, C. Jin, J. Hu, R. Thomale, K. Sumida, S. Wu, K. Miyamoto *et al.*, Nat. Phys. **15**, 41 (2019).
[51] D. Wang, L. Kong, P. Fan, H. Chen, S. Zhu, W. Liu, L. Cao, Y. Sun, S. Du, J. Schneeloch, R. Zhong, G. Gu, L. Fu, H. Ding, and H.-J. Gao, Science **362**, 333 (2018).

[52] L. Kong, S. Zhu, M. Papaj, H. Chen, L. Cao, H. Isobe, Y. Xing, W. Liu, D. Wang, P. Fan, Y. Sun, S. Du, J. Schneeloch, R. Zhong, G. Gu, L. Fu, H.-J. Gao, and H. Ding, Nat. Phys. **15**, 1181 (2019).

[53] S. Zhu, L. Kong, L. Cao, H. Chen, M. Papaj, S. Du, Y. Xing, W. Liu, D. Wang, C. Shen, F. Yang, J. Schneeloch, R. Zhong, G. Gu, L. Fu, Y.-Y. Zhang, H. Ding, and H.-J. Gao, Science **367**, 189 (2020).

[54] W. Liu, L. Cao, S. Zhu, L. Kong, G. Wang, M. Papaj, P. Zhang, Y.-B. Liu, H. Chen, G. Li, F. Yang, T. Kondo, S. Du, G.-H. Cao, S. Shin, L. Fu, Z. Yin, H.-J. Gao, and H. Ding, Nat. Commun. **11**, 5688 (2020).

[55] S. Bhattacharyya, G. Akhgar, M. Gebert, J. Karel, M. T. Edmonds, and M. S. Fuhrer, Adv. Mater. **33**, 2007795 (2021).

[56] T. M. Schmidt, R. H. Miwa, and A. Fazzio, Phys. Rev. B **84**, 245418 (2011).

[57] J. Henk, M. Flieger, I. V. Maznichenko, I. Mertig, A. Ernst, S. V. Eremeev, and E. V. Chulkov, Phys. Rev. Lett. **109**, 076801 (2012).